IEEE ComSoc IEEE Communications Society | IEEE COMPUTER SOCIETY | IEEE Signal Processing Society | VTS | IEEE Transactions on Machine Learning in Communications and Networking

Received 27 October 2022; revised 5 February 2023, 2 April 2023, and 11 May 2023; accepted 11 June 2023.
Date of publication 15 June 2023; date of current version 6 December 2023.

The associate editor coordinating the review of this article and approving it for publication was Z. Yang.

Digital Object Identifier 10.1109/TMLCN.2023.3286793

Deep Learning Forecasting and Statistical Modeling for Q/V-Band LEO Satellite Channels

BASSEL AL HOMSSI[1] (Member, IEEE), CHIU C. CHAN[1], KE WANG[1], WAYNE ROWE[1] (Member, IEEE), BEN ALLEN[2,3], BEN MOORES[2], LÁSZLÓ CSURGAI-HORVÁTH[4], FERNANDO PÉREZ FONTÁN[5], SITHAMPARANATHAN KANDEEPAN[1], AND AKRAM AL-HOURANI[1]

[1]Department of Electrical and Electronic Engineering, RMIT University, Melbourne, VIC 3000, Australia
[2]OneWeb, W12 7FQ London, U.K.
[3]Electronic Engineering, The University of Surrey, GU2 7XH Guildford, U.K.
[4]Department of Broadband Infocommunications and Electromagnetic Theory, Budapest University of Technology and Economics, 1111 Budapest, Hungary
[5]Telecommunications Engineering School, The University of Vigo, 36310 Vigo, Spain

Corresponding author: B. A. Homssi (bhomssi@ieee.org)

This work was supported in part by the United Kingdom (U.K.)-Australia Space Bridge, a collaboration between Catapult, SmartSat Cooperative Research Centre (CRC), Australian Government, and U.K. Government (V-Band Radio Channel Prediction for Next Generation Low Earth Orbit (LEO) Constellations) under Grant P4-22; and in part by Vigo has been gathered in the course of Project Information-Centric sAtellite-netwoRk for vehicUlar communicationS (ICARUS) under Grant PID2020-113240RB-I00 and Grant MCIN/AEI/10.13039/501100011033.

ABSTRACT As the number of satellite networks increases, the radio spectrum is becoming more congested, prompting the need to explore higher frequencies. However, it is more difficult to operate at higher frequencies due to severe impairments caused by varying atmospheric conditions. Hence, radio channel forecasting is crucial for operators to adjust and maintain the link's quality. This paper presents a practical approach for Q/V-band modeling for low Earth orbit satellite channels based on tools from machine learning and statistical modeling. The developed Q/V-band LEO satellite channel model is composed of: 1) forecasting method using model-based deep learning, intended for real-time operation of satellite terminals; and 2) statistical channel simulator that generates a time-series path-loss random process, intended for system design and research. Both approaches capitalize on real-measurements obtained from AlphaSat's Q/V-band transmitter at different geographic latitudes. The results show that model-based deep learning can outperform simple statistical and deep learning methods by at least 50%. Moreover, the model is capable of incorporating varying rain and elevation angle profiles.

INDEX TERMS LEO satellites, time-series prediction, machine learning, artificial intelligence, LSTM, rain fading, radio channel modeling, Q/V-band.

I. INTRODUCTION

THE rise of the new commercial space-age has proclaimed the evolution of communication systems through the emergence of next-generation dense low Earth orbit (LEO) constellations. The deployment of these constellations strive to fulfill the global connectivity promise, ultimately striding towards access equality [1]. Service providers are therefore required to upgrade their capacities to provide adequate bandwidth that accommodates the anticipated increase in user traffic. However, the radio spectrum is becoming increasingly congested, where the C-, and Ku-bands are currently near their limit and the Ka-band is rapidly being occupied [2]. New spectral regions in the Q/V-band are seen as the new frontier for LEO networks [3], [4], offering multifaceted advantages over lower frequencies with a wider usable bandwidth for supporting higher data rates, a precise satellite footprint leading to lower co-channel interference, and reduction in components size resulting in lower installation and deployment costs.

Despite the improved spectrum availability and the increased bandwidth offered by higher frequency bands, maintaining the quality of service (QoS) becomes more

challenging. This is primarily because of the increased tropospheric propagation impairments in both the attenuation magnitude and fading variability compared to lower frequencies [5]. As such, simply increasing the equivalent isotropic radiated power (EIRP) does not solve the problem, mainly because of the rapid changes in propagation conditions in the troposphere. As a result, it is very challenging, and in some cases impossible to maintain the link connectivity under severe weather conditions [6]. Hence, it is essential for the service provider to be able to predict and adjust the different network parameters to maintain seamless service. Adjustments can be in the form of reverting to lower frequencies, changing the modulation and coding scheme, or handover to terrestrial or alternative non-terrestrial routes such that the link is restored.

The need for proactive networks is even more critical in LEO constellations because, contrary to geostationary (GEO) links, they are characterized by rapid relative movement with respect to ground terminals. As such, the elevation angle is continuously varying resulting in signal envelope variations due to interaction with both the clutter and the atmospheric effects. While the satellite passes are predictable in the short-term and thus are approximated using methods such as the two-line element, the channel variations are challenging to predict and require more complex techniques [7].

A. RELATED WORK

In any satellite communication link, the vast majority of signal propagation occurs under free-space conditions and only interacts with the clutter near the ground [8]. These interactions entail multi-path fading, signal shadowing, air absorption, and rain fading [9]. The extent of these interactions vary depending on the operating frequency band. A plethora of channel models that capture those different interactions are well-established for lower frequencies (L/S/C/Ku)-bands. As the frequency of operation increases beyond the Ka-band, the effect of fading on the signal due to atmospheric and rain absorption significantly increases [5]. To understand the effects of different weather conditions in high frequencies, researchers conduct measurement campaigns for different high frequency links. The authors in [10] derive empirical models based on collected measurements for a 38 GHz terrestrial link under different weather conditions. In addition, Q/V-band measurements collected for AlphaSat [11] and ItalSat [12], are similarly utilized to develop empirical models that capture the effect of rain fading [13]. However, the majority of these models are geography-specific, i.e., they depend on empirical fitting and cannot be projected onto other geographical locations. In order to overcome this limitation, researchers resort to fit measurements that are obtained in different locations [14] at the cost of increased prediction error.

Conventionally, statistical modeling is utilized to model rain attenuation. Such models utilize weather statistics over extended periods of time, capturing the channel long-term variations. Details of such models are provided in [15] and references therein. Moreover, statistical models are the default method adopted in the recommendations by the International Telecommunication Union (ITU). They specifically

TABLE 1. List of symbols.

Parameter	Symbol	Unit
Air absorption	η_{a}	dB
Autocorrelation function	$\hat{R}$	-
Average sea height	h_{s}	km
Carrier frequency	f_c	Hz
Correlation filter impulse response	h_{cor}	-
Correlated EPL mean	μ_{Y_η}	dB
Correlated EPL random process	Y_η	dB
Correlated EPL standard deviation	σ_{Y_η}	dB
Correlation time factor	τ_{cor}	s
Distance from ground station to satellite	d	m
Earth average radius	$R_\oplus$	m
Elevation angle	θ	$^\circ$
Excess path loss (EPL)	η	dB
Free-space path loss	l	dB
Gate activation function	σ_{g}	-
Hyperbolic tangent function	σ_{c}	-
LSTM bias weights	b	-
LSTM cell at time t	c_t	-
LSTM cell feature function at time t	$\tilde{c}_t$	-
LSTM cell input function at time t	x_t	-
LSTM cell output at time t	y_t	-
LSTM forget gate function at time t	f_t	-
LSTM input gate at time t	i_t	-
LSTM input weights	W	-
LSTM input vector	X_n	-
LSTM recurrent weights	U	-
LSTM output gate function at time t	o_t	-
LSTM output vector	Y_n	-
Measured EPL	$\tilde{\eta}$	dB
Model parameters	$c_{\{1,2,3,4,5\}}$	-
Predicted EPL	$\hat{\eta}$	dB
Prediction window samples	W	samples
Rain height	h_{r}	km
Rain horizontal distance	L_{G}	km
Rain fading	η_{r}	dB
Rain fading coefficient	k	-
Rain fading coefficient	α	-
Rain fading mean	μ	dB
Rain fading standard deviation	σ	dB
Rain rate	R	mm/hr
Rain slant distance	L_{s}	km
Received power at the terminal	P_{r}	dBm
Receiver's antenna gain	G_{r}	dB
Satellite altitude	h	m
Satellite altitude to center	a	m
Satellite transmit EIRP	P_{t}	dBm
Time	t	s
Time delay	τ	s
Training input mean	$\bar{X}_{\mathrm{tr}}$	-
Training input vector	X_{tr}	-

TABLE 1. ***(Continued.)*** **List of symbols.**

Training input sequence standard deviation	$s_{X_{\mathrm{tr}}}$	-
Training output mean	$\bar{Y}_{\mathrm{tr}}$	-
Training output sequence standard deviation	$s_{Y_{\mathrm{tr}}}$	-
Training output vector	Y_{tr}	-
Uncorrelated EPL random process	X_{η}	dB

capture link attenuation due to atmospheric gases, cloud, and fog for frequencies higher than 10 GHz [16], [17], [18]. Moreover, the third generation partnership (3GPP) follows a similar approach to model the rain attenuation statistically [19]. In [20], several statistical rain attenuation models are assessed for the Ka-band. While the analysis shows that the ITU-R P.618 model provides the most adequate prediction, it is still limited due to possible shifts in rain patterns, especially in tropical regions. To enhance the model, the ITU-R channel model is modified in [21] to tailor for LEO links where a novel model that utilizes exponential rain cell profiles and rain rate adjustment factors in introduced. However, statistical models can only provide long-term predictions and do not feature the temporal correlation present in the channel, rendering short-term, i.e., duration of tens of milliseconds to a few seconds only, prediction inadequate.

The lack of short-term prediction capabilities has prompted researchers to investigate stochastic dynamic models (SDM) for rain attenuation prediction. SDMs are mainly deployed to solve dynamic decision-making problems, where they rely on time-varying stimulus information to generate a stochastic process. SDMs incorporate rain fading correlation with respect to time [22]. Unlike statistical methods, SDMs provide an inherent compatibility with LEO satellites, whereby the time-varying elevation angle can be easily incorporated in the model [23]. Through their ability to derive both first- and second-order statistics, SDMs provide a prediction model with higher robustness to channel fluctuations, detailed in [24] and references therein. While SDMs can depict the time correlation, they fundamentally generate a stochastic process, which cannot be used in active links that rely on real-time prediction. Hence, SDMs rely on synthetic rain data which is typically generated by using an uncorrelated random variable generator, e.g., log-normal model. As a result, the rain data used as an input is not correlated in time, however, rain is a highly correlated event with respect to time, whereby the rain probability is much higher at certain months of the year.

Another statistical approach that is widely adopted for time-series prediction is the auto-regressive integrated moving average (ARIMA). ARIMA combines auto-regressive models that provide data time correlation and the moving average information to provide an approximated time-series prediction [25]. An ARIMA channel model for predicting the rain attenuation recorded for 28 GHz in Surabaya is discussed in [26]. Although the model provides accurate prediction, it is location specific. Nevertheless, it provides a generic framework for ARIMA-based rain fading modeling for satellite channels. Regression methods, however, are not very accurate since they are not well-equipped to predict rapid variations since they are based on averages.

Another approach to short-term forecasting is using machine learning-based algorithms [27]. Using machine learning techniques, the predictor network can, in real-time, forecast the channel and allow the network to adjust its parameters accordingly and provide its users with a seamless service. In [28], a back-propagation neural network has been used to predict the rain rate and corresponding attenuation, however it has not been tested for higher frequency bands where channel fluctuations are significantly higher. In [29], synthetic rain data is generated and utilized to train a long short-term memory (LSTM) neural network. The model used provided promising results in terms of rain attenuation prediction. The authors in [30] utilize an artificial neural networks (ANN) to classify the effects of the weather on a Q/V-band channel using real measurements from ItalSat. This is further enhanced by the same authors by adding an LSTM layer post-classification to provide more accurate forecasting [31]. Nevertheless, these models do not depict the effect of elevation angle and the accuracy of the models start to degrade as the prediction window increases.

B. CONTRIBUTIONS AND OUTCOMES

This article presents a Q/V-band LEO satellite channel model as follows; (i) a real-time forecasting method using model-based deep learning and (ii) a statistical channel simulator for channel modeling and system development. The main contributions of this work are summarized as follows.

- We present a statistical modeling approach that captures the impact of rain fading incorporating the time-varying element of LEO satellites and rain rate.
  - Contrary to existing satellite channel models that address GEO satellite links [15], we develop a model that is suitable for the dynamic nature of LEO satellite links. Namely, the model takes into account the varying elevation angle characteristic of LEO satellite links which directly impacts the amount and variability of attenuation caused by the rain.
  - Contrary to the commonly used models provided by the ITU [17], [32] which captures the fading using the average only, we depict the fading as a normal-distributed random process characterized not only by its time-varying average but also by a time-varying standard deviation.
- We develop a model-based deep learning LSTM network that is capable of real-time forecasting for Q/V-band LEO satellite channels. The proposed model-based deep learning LSTM network capitalizes on the statistical rain attenuation model to achieve more adequate long-term prediction.
  - Contrary to existing works [30], [31], which also proposed the concept of using AI for time-series forecasting of Q/V-band channels, our proposed

modeling approach does not require a weather classification network prior to the LSTM layer.
  - In comparison to existing works [31], [33], [34], which present the use of LSTM networks for time-series forecasting, our proposed architecture provides more accurate forecasting as the prediction window increases.
  - Contrary to existing satellite channel prediction works [15], [31], which heavily feature geostationary links, the proposed model-based deep learning approach extends its modeling to links with time-varying elevation angle profiles making it an ideal candidate for real-time prediction for LEO satellite channels.
- We devise a time-correlated statistical channel model for the generation of time-series for Q/V-band LEO satellite channels. The proposed model relies on the statistical modeling of the rain fading and a correlation filter that introduces correlation in the time-series.

The rest of this paper is organized as follows. Section II presents the LEO satellite channel path loss modeling approach and details the statistical rain fading model proposed. Section III proposes the real-time deep learning LSTM model and the different layers it incorporates. Section IV details the time-correlated satellite channel model. Section V outlines the measurements used to validate the models and the prediction results, while Section VI provides concluding remarks.

II. SATELLITE PATH LOSS MODEL

We consider the downlink between a LEO satellite transmitting with a constant EIRP, denoted as P_t, to a ground station with a receiver antenna gain, denoted as G_r, we assume that the ground station can always track the satellite with an accuracy such that the gain is always maintained at its maximum. Accordingly, the received power at the ground station is obtained as follows

$$P_r[\text{dBm}] = P_t[\text{dBm}] + G_r[\text{dB}] - l[\text{dB}] - \eta[\text{dB}], \quad (1)$$

where l is the free-space path loss (FSPL) and η is the excess path loss (EPL).

Since LEO satellites are continuously orbiting Earth, the elevation angle is constantly changing with respect to a user terminal on the ground. Accordingly, the FSPL is a function of the elevation angle as follows

$$l(\theta)[\text{dB}] = 20\log_{10} d(\theta) + 20\log_{10} f_c - 147.55, \quad (2)$$

where f_c is the carrier frequency and d is the instantaneous distance. By approximating Earth to an ideal sphere (i.e. without oblateness), the distance can be approximated as follows

$$d(\theta) = \sqrt{R_\oplus^2 + a^2 - 2R_\oplus a \sin\left(\theta + \text{asin}\left[\frac{R_\oplus}{a}\cos\theta\right]\right)}, \quad (3)$$

where θ represents the elevation angle, $R_\oplus$ is the Earth's average radius, $a = R_\oplus + h$, and h is the satellite altitude above the sea mean level. The derivation of (3) is presented in Appendix A.

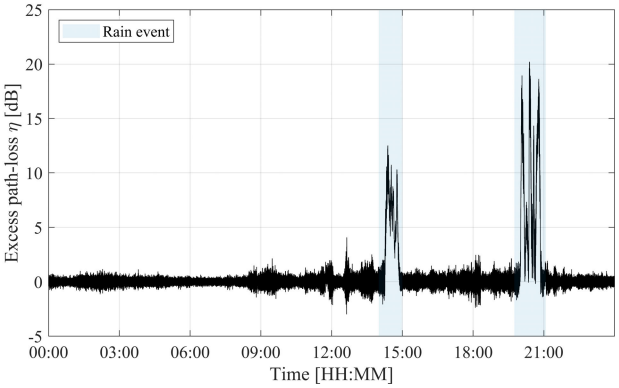

FIGURE 1. An example of the measured EPL time-series for Q-band showcasing the effect of rain. Measurements are for AlphaSat recorded at the ground station in Vigo with an elevation of 30.6° on 6th of July 2017.

The EPL is the additional power loss due to impairments such as gas absorption, rain fading, and shadowed multi-path fading [35]. In practice, for high frequencies such as the Q/V-band, the link is only established under line-of-sight (LoS) conditions and thus impairments due to clutter shadowing and multi-path fading can be ignored because of the high directivity of the antenna. Hence, the total EPL is composed of multiple parts as follows

$$\eta(\theta) = \eta_a(\theta) + \eta_c(\theta) + \eta_r(\theta), \quad (4)$$

where η_a, η_c, and η_r are the excess power loss due to air absorption, cloud attenuation, and rain fading respectively. Depending on the weather conditions, the EPL can reach very high levels (exceeding 20 dB) as illustrated by measurements shown in Fig. 1.

A. ATMOSPHERIC ABSORPTION

Losses due to atmospheric absorption refers to the losses generated when atmospheric gases absorb the energy of the signals that interact with the gas molecules. Losses due to atmospheric absorption vary with both the frequency and the length of propagation path, i.e., varies for different elevation angles. A detailed model that utilizes the layered estimation of the atmosphere is defined in ITU-R P.676 [16] providing a geometric calculation methodology to obtain the air absorption for different frequencies under various elevation angles. Fig. 2 illustrates the atmospheric absorption path loss for frequencies ranging from 0-100 GHz for selected elevation angles.

B. CLOUD ATTENUATION

Another type of attenuation that becomes significant at high frequencies is the cloud attenuation. Similar to the atmospheric absorption, the cloud attenuation is highly dependent on the elevation angle of the link. Moreover, other parameters contribute such as the temperature and specific attenuation coefficient which is typically between 1-3 (dB/km)/(g/m^3) in

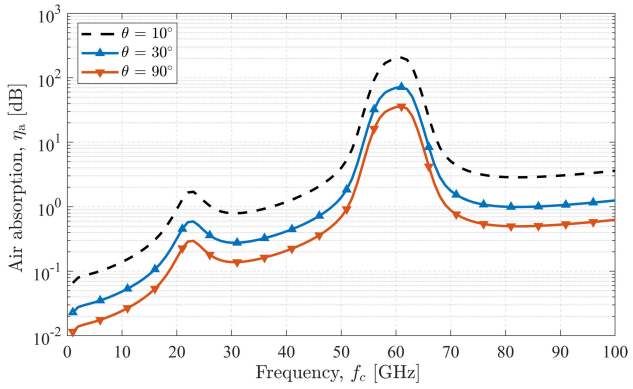

FIGURE 2. Atmospheric absorption as a function of frequency and for different elevation angles calculated from the model derived in [36]. The approximate water vapor density is calculated according to Eq. 6 in ITU-R P.835-2 model with standard ground vapor density 7.5 g/m^3 and altitude of 2 km [37].

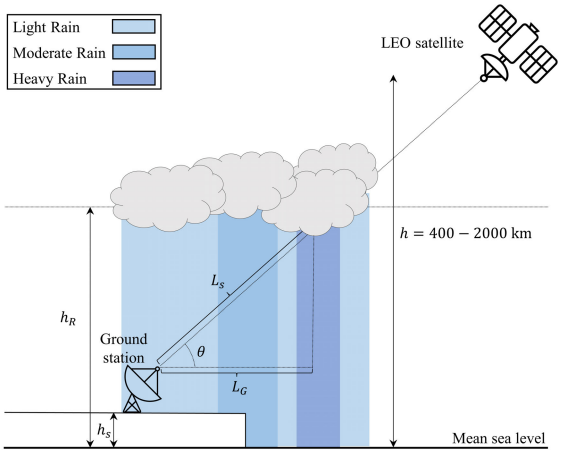

FIGURE 3. Rain geometric model, for a typical LEO satellite (400 - 2000 km), showing a non-homogeneous rain, height, and cloud thickness. Rain color shade represents the rain rate level (darker corresponds to heavier rain).

the Q/V-band [18]. We address the effect of cloud distribution and incorporate their effect within the rain attenuation variance in (5).

C. RAIN ATTENUATION

Rain attenuation is very severe in transmissions that utilize the V-band, as illustrated in Fig. 1, where the attenuation due to rain can exceed 20 dB in some cases. In the case of LEO links, rain attenuation is contingent on both the amount of rain (rain rate) and the signal path length (elevation angle), both of which are time dependent. Moreover, rain is an event that is probabilistic in nature and depends on several interconnected factors such as the cloud thickness and size, temperature and precipitation levels in the atmosphere. Modeling the attenuation of the signal power due to rain is extensively studied in the literature whereby many models that rely on empirical, statistical, and learning approaches are available [15].

The attenuation caused by the rain is also not deterministic for a given rain rate, denoted by R and measured in mm/hr, and thus ideal geometric models that are usually featured in the literature are not very accurate. This is due to over-simplifications such as, the rain height is assumed to be constant, the cloud thickness as identical, and the rain rate as uniform across the different clouds. On the other hand, the variance in the fading is due to the spatial inhomogeneity of the rain rate along the link and the impact of the drop size distribution. A more realistic scenario is illustrated in Fig. 3, however is very difficult to model since the rain height, cloud thickness, and rain rate are stochastic in nature. To overcome some of these simplifications, we propose to capture the rain attenuation as a random process that follows a normal distribution as follows

$$\eta_{\mathrm{r}}(\theta) \sim \mathcal{N}(\mu(R,\theta), \sigma(R,\theta)), \tag{5}$$

where μ and σ are the rain attenuation average and standard deviation parameters, measured in decibels. Both parameters are a function of the rain intensity, illustrated in Fig. 4, where both increase as the rain rate increases for a fixed elevation angle, the rain attenuation EPL is typically depicted in the literature with its average only. In this case the standard deviation can compensate for the non-homogeneous nature of the system.

Unlike in terrestrial links, only a small portion of a satellite communication link is impacted by rain which depends on the path length through atmosphere and consequently the elevation angle. As a result, in order to model the rain fading mean, we need to account for the slant distance, denoted with L_{s}, which corresponds to the actual path-length impacted by the rain as illustrated in Fig. 3. Accordingly, the average rain attenuation is the rain rate multiplied by the *effective rain distance* [17] as follows

$$\mu(r,\theta) = c_1 k R^{\alpha} (h_{\mathrm{r}} - h_{\mathrm{s}}) \csc\theta, \tag{6}$$

where k and α are empirical parameters obtained for different frequencies, elevation, and tilt angles [32], h_{r} and h_{s} are the rain and receiver heights with reference to the mean sea level respectively, and c_1 is the reduction factor. In practice, the reduction factor is empirically obtained due to its dependence on many incorporated factors such as the receiver geographic location [15].

In our proposed approach, we model the variability in rain attenuation for a given rain rate using both the mean and the standard deviation parameters. Contrary to typical methods which only consider the mean, we also capture the standard deviation as a function of the horizontal rain distance, L_{G}, as illustrated in Fig. 3. This is because the smaller the horizontal distance, the less likely that the signal will fall under another rain cell and thus will have more homogeneous rain behaviour. With the aid of empirical fitting, we model the standard deviation as follows

$$\sigma(r,\theta) = c_2 R^{c_3} (h_{\mathrm{r}} - h_{\mathrm{s}}) \cot\theta, \tag{7}$$

where c_2 and c_3 are constants obtained using fitting and are dependant on the local climate. Note that as the rain

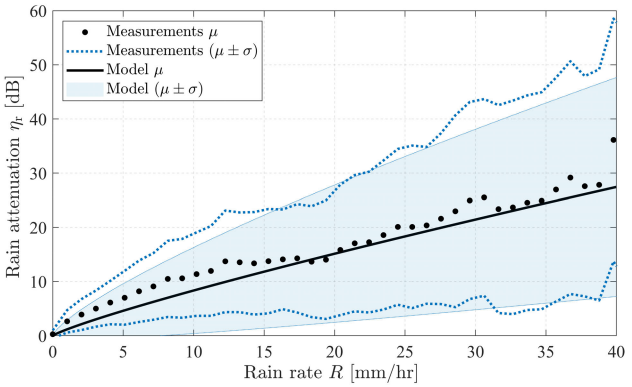

FIGURE 4. Realization of the proposed long-term statistical rain attenuation modeling using both the EPL average and standard deviation compared to AlphaSat Q/V-band measurements collected at Chilbolton, detailed in Sec. V.

rate increases, the standard deviation increases as well, this can be accounted due to the presence of larger and nonuniform clouds, the increase in dispersion of rain droplet sizes, and the increase of rain height [15]. In addition, higher elevation angles result in a shorter horizontal distance thus reducing the standard deviation of the power fading. The reasoning for both (6) and (7) are further explained in Appendix B.

III. SATELLITE CHANNEL TIME-SERIES FORECASTING

In this section, we present a real-time predictor using model-based deep learning that combines both long- and short-term characteristics of the channel to obtain more accurate forecasting. This is achieved by guiding a deep learning LSTM network with the statistical modeling presented in Sec. II. The accuracy of the forecasting can be significantly enhanced by incorporating long-term statistics of the rain rate along with the neural network, as illustrated in Fig. 5. This is particularly helpful for practical links where a LEO ground terminal is expected to have access to real-time measurements of the following parameters,

1) Satellite ephemeris (historic and future): LEO satellites move in a dynamic motion with respect to the ground terminal and are therefore have a rapidly changing elevation angle. Ground terminals can accurately estimate the satellite pass using methods such as two-line elements, or satellite ephemeris.
2) Varying rain rate (historic): Rain rate affects the long-term aspect of the channel whereby higher rates lead to higher EPL and higher EPL variation. The ground terminal can have access to real-time measurements of the rain rate if a rain sensor is installed, or can have less-frequent rain data obtained from weather monitoring services.
3) Path loss measurements (current): The current measured EPL of the communication link, where the ground terminal has access to real-time measurements of the channel.

A. MODEL-BASED LSTM ARCHITECTURE

Due to their inherent sequence detection ability, LSTM networks can provide accurate prediction especially for short-term forecasting which is highly correlated in time. To enhance the LSTM network capabilities for longer prediction windows, we utilize a novel model-based LSTM architecture that takes into account the rain statistics. The model-based LSTM network architecture consists of four main layers; (i) an input layer, (ii) LSTM layer, (iii) regression layer, and (iv) the output layer.

1) INPUT LAYER

The input layer is responsible for injecting the different input features represented by the input state vector, denoted with X_n where n is the sample index. The input state vector consists of three main entries; the current EPL, the predicted statistical average, and the predicted standard deviation. The input vector is first scaled (standardized) with respect to the average and standard deviation of the training input, denoted with $\bar{X}_{\text{tr}}$ and $s_{X_{\text{tr}}}$ respectively. Note that the training procedure is detailed in Sec. III-B. Assuming that the measurements are sampled at a sampling rate of T_s, then the input array to the model-based LSTM is constructed as follows

$$X_n = \frac{\begin{bmatrix} \tilde{\eta}_n \\ \mu_{n+1} \\ \sigma_{n+1} \end{bmatrix} - \bar{X}_{\text{tr}}}{s_{X_{\text{tr}}}}, \tag{8}$$

where $\tilde{\eta}$ is the measured EPL.

2) LSTM LAYER

This portion of the network holds the different LSTM units. Each unit is composed of a cell and three gates; input, forget, and output gates. The cell is the memory component and the gates are responsible for regulating the flow of information into the cell. The equations to calculate the input (i), forget (f), and output (o) gates are formulated as follows [38]

$$\begin{bmatrix} i_t \\ f_t \\ o_t \end{bmatrix} = \sigma_{\text{g}} \left(\begin{bmatrix} W_i \\ W_f \\ W_o \end{bmatrix} x_t + \begin{bmatrix} U_i \\ U_f \\ U_o \end{bmatrix} y_{t-1} + \begin{bmatrix} b_i, \\ b_f, \\ b_o, \end{bmatrix} \right) \tag{9}$$

where x and y are the input and output vectors at a time instant t, $\sigma_{\text{g}}(\cdot)$ is the gate activation function defined as a sigmoid given as $\sigma_{\text{g}}(x) = (1 + e^{-x})^{-1}$, and W_i,W_f, W_o and U_i, U_f, U_o and b_i, b_f, b_o are the input, recurrent, and bias weights for the input, forget, and output gates respectively. Moreover, the cell input activation equation responsible for the feature extraction is calculated similarly as follows [38]

$$\tilde{c}_t = \sigma_{\text{c}}(W_g x_t + U_g y_{t-1} + b_g), \tag{10}$$

where $\sigma_{\text{c}}(\cdot)$ is the hyperbolic tangent function $\sigma_{\text{c}}(x) = \tanh(x)$, and W_g, U_g and b_g are the input, recurrent, and bias weights for the cell activation. Accordingly, the cell state is calculated as follows [38]

$$c_t = f_t \odot c_{t-1} + i_t \odot \tilde{c}_t, \tag{11}$$

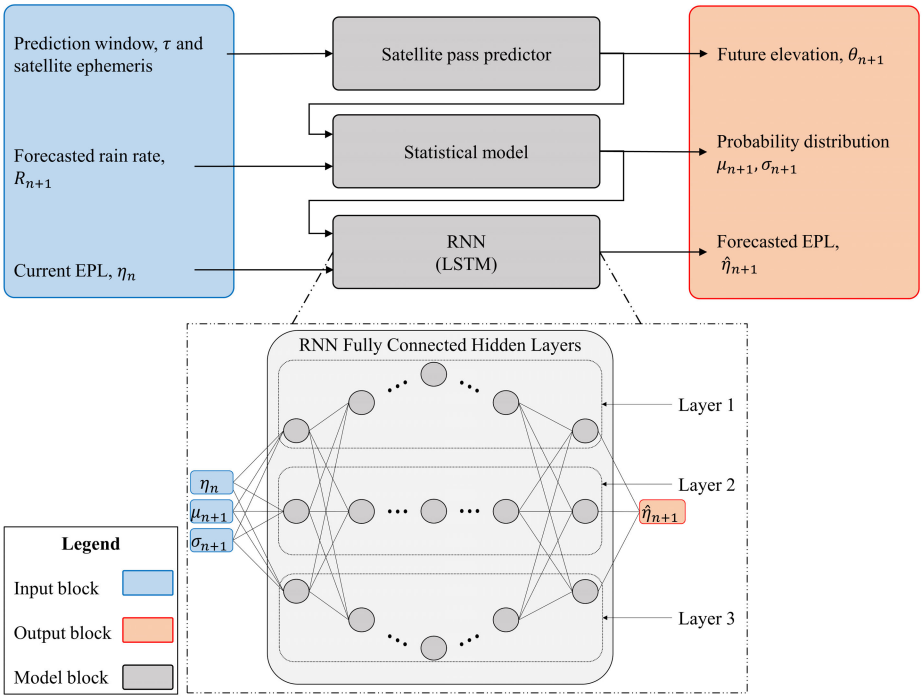

FIGURE 5. A high-level abstract of the proposed real-time forecasting using model-based deep learning LSTM for Q/V-band LEO links.

where $\odot$ denotes the Hadamard product or element-wise product. Finally, the output of the unit is obtained as follows [38]

$$y_t = o_t \odot \sigma_c(c_t). \tag{12}$$

The LSTM layer utilized in this model consists of a deep learning LSTM with three layers, 64 forward LSTM units in the first layer, followed by another 64 forward LSTM units in the second layer. A zoomed illustration of each LSTM unit is shown in Fig. 6.

3) REGRESSION LAYER

The layer is responsible for calculating the regression loss function. Since the application of this layer is for sequence regression, then the loss function is the mean square error (MSE) and is calculated as follows

$$\text{loss} = \frac{1}{M}\sum_{i=1}^{M}(t_i - y_i)^2, \tag{13}$$

where y_i is the predicted output and t_i is the target output and M is the total number of responses.

4) OUTPUT LAYER

This layer is responsible for de-standardizing the output vector, denoted by Y_n. Accordingly, the model-based LSTM predicted EPL is obtained from the output as follows

$$\hat{\eta}_{n+1} = s_{Y_{\text{tr}}} Y_n + \bar{Y}_{\text{tr}}, \tag{14}$$

where $\bar{Y}_{\text{tr}}$ and $s_{Y_{\text{tr}}}$ are the target vector mean and standard deviation respectively.

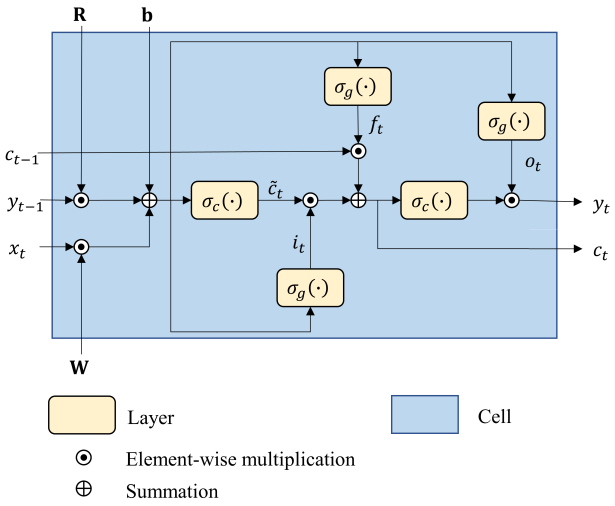

FIGURE 6. An illustration of the different components and hidden layers within a typical LSTM cell. LSTM cells take into account the previous cell state and output, and incorporate their values in the calculation of the new state and output.

B. MODEL-BASED LSTM TRAINING AND TESTING

The dataset required to train the model-based LSTM network is composed of three time-series; (i) EPL measurements, (ii) rain rate, and (iii) the elevation angle between the satellite and ground station. The rain rate and elevation angle time-series are used to obtain the average and standard deviation time-series from (6) and (7) respectively. The training

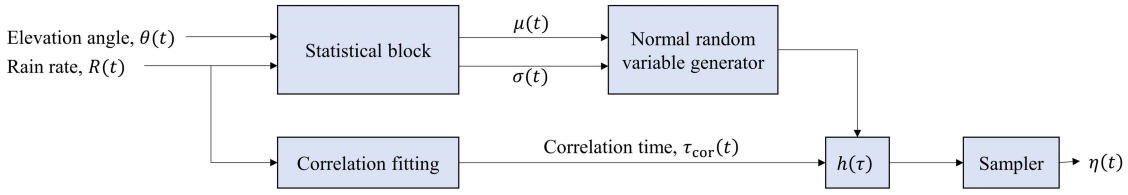

FIGURE 7. Block diagram of the channel predictor (simulator) for the modeling scenario. The filter utilizes an exponentially determined by means of curve fitting correlation time factor τ_{cor}.

data is split into 90% training samples and 10% for testing samples.

1) TRAINING

It is more convenient to do the training in an offline mode after the measurements were being collected. Assuming that the training data has a length of M samples, then the input training matrix is generated as follows

$$X_{\text{tr}} = \begin{bmatrix} \eta_1, \ldots, \eta_{M-1} \\ \mu_2, \ldots, \mu_M \\ \sigma_2, \ldots, \sigma_M \end{bmatrix} \tag{15}$$

where μ and σ are always a sample ahead because they are used to predict the EPL. On the other hand, the target vector is generated as $Y_{\text{tr}} = \{\eta_2, \ldots, \eta_M\}$. Prior to training the network, both the input matrix and target vectors are standardized in order to enhance the efficiency. The input matrix is standardized by subtracting its mean, $\bar{X}_{\text{tr}}$, and then dividing by its standard deviation, $s_{X_{\text{tr}}}$. Similarly, the target vector is standardized by subtracting its mean $\bar{Y}_{\text{tr}}$, followed by dividing it by its standard deviation, $s_{Y_{\text{tr}}}$. The network is trained using a total of 100 epochs using the Adam optimization algorithm [39].

2) TESTING

The testing is achieved by passing the testing proportion of the measurements that are still *blind* to the network. These measurements should range in fading severity, rain rate variations, and elevation profile in order to determine the accuracy of the network. Similar to the training dataset, the testing measurements need to be standardized using the mean and standard deviation of the training set as discussed in the training procedure above.

C. IMPLEMENTATION DETAILS

The proposed machine learning prediction algorithm was developed using MATLAB scripting, whereby both the deep learning [40], parallel computing [41], and statistics and machine learning [42] toolboxes were utilized. The system used for the experimentation has a 16-logical core Intel Xeon CPU at 3.2 GHz and an Nvidia Quadro 4000 GPU. The source code for the trained machine learning model is also provided on GitHub [43].

IV. SATELLITE CHANNEL TIME-SERIES GENERATION

For cases where there is no access to real-time measurements, synthetic data emulating radio channel characteristics can provide a viable route for scenario simulation and network modeling. In order to incorporate realistic temporal correlation in the EPL, we develop a Q/V-band LEO satellite statistical channel model that modifies an uncorrelated time-series by passing it through a correlation filter as illustrated in Fig. 7.

Unlike the real-time predictor presented in Sec. III, the statistical time-series generator only requires two inputs; (i) the elevation angle and (ii) the rain rate data. The generator follows the statistical model detailed in Sec. II where both the time-varying elevation angle and rain rate are utilized to derive the distribution parameters; the mean and standard deviation obtained from (6) and (7) respectively. Both parameters are then fed into a pseudo-random variable (RV) generator (e.g., Mersenne Twister [44]) to generate an independent and uncorrelated normally distributed random process, denoted by $X_{\eta_r}(t, \tau)$ where τ corresponds to the random variable index. Then, the RV samples are passed through the correlation filter that incorporates temporal correlation in the generated EPL time-series.

In typical scenarios, the correlation of the EPL time-series decreases with time, resulting in a decaying autocorrelation function. We follow the assumption established in [22] where the decay is modeled using an exponential fit as follows

$$\hat{R}(\tau) = \exp\left(-\frac{\tau}{\tau_{\text{cor}}}\right), \tag{16}$$

where τ is the delay and τ_{cor} is the correlation time factor of the channel. The correlation time factor captures the effect of the holding time of the channel, i.e., for larger correlation constant the fading exhibits longer temporal correlation. In the case of rain attenuation EPL, the correlation time magnitude is assumed to be solely dependent on the rain rate, whereby the correlation time is expected to be inversely related to the variations in the signal strength. This is similar to channel coherent time in multi-path fading where higher signal variations lead to a reduced coherent time. Note that as the elevation angle decreases, the more the link starts to behave like a terrestrial link whereby the horizontal elements becomes more dominant. This means that the transmission passes through more rain and thus the time-correlation increases. However, due to lack of measurements for LEO satellites in the Q/V-band, we restrict the correlation to be a function of the rain.

FIGURE 8. Photos of the Q/V-band ground stations used in each of the three sites; (a) Chilbolton, (b) Vigo, and (c) Budapest.

The uncorrelated RV samples are passed through a correlation filter in order to introduce the appropriate correlation in the time-series. The chosen filter model depends on the nature of correlation that the channel has (e.g., Jakes filter is used to model the correlation for multi-path fading for land mobile satellite channels in ITU-R P.681 [45]). The resulting filter impulse response is obtained for an exponential auto-correlation model as follows

$$h_{\text{cor}}(t,\tau) = \left(\frac{2}{\pi}\right)^{\frac{3}{4}} \frac{1}{\sqrt{\tau_{\text{cor}}(t)}} I_0\left(\frac{\tau}{\tau_{\text{cor}}(t)}\right) \tag{17}$$

where $I_0(\cdot)$ is the modified Bessel function of the first kind. Note that the correlation time is not constant since the rain profile is time-varying. While the output $Y_\eta(t,\tau)$ is now correlated, the filter does not preserve its mean and standard deviation. Hence, a scaling operation is required to retain the statistics of the RV as follows

$$\hat{\eta}(t,\tau) = \mu(t) + \sigma(t)\left(\frac{Y_\eta(t,\tau) - \mu_{Y_\eta}(t)}{\sigma_{Y_\eta}(t)}\right), \tag{18}$$

where $\mu_{Y_\eta}(t)$ and $\sigma_{Y_\eta}(t)$ are the time-varying mean and standard deviation of the correlated output $Y_\eta(t,\tau)$ respectively. Since we are interested in the EPL in the time-domain only, a sampler is added to sample the random process as shown in Fig. 7.

V. CHANNEL MEASUREMENTS AND RESULTS

Since there are currently no LEO satellites with Q/V-band payload that is publicly available, we have utilized GEO measurement campaigns with ground stations at several geographical locations to capture the varying elevation angle effect. In this work, we exploit the Q/V-band (at frequency 39.04 GHz) by utilizing measurements collected via the experimental payload on-board AlphaSat from three different sites (Chilbolton, Vigo, and Budapest). Photos of the ground stations at the three different sites are shown in Fig. 8. The different campaign parameters are summarized in Table. 2 for each site including the corresponding elevation angles.

A. MEASUREMENT DATA-SETS

The collected measurements represent the EPL measured by the ground station as a function of time. This is achieved by calculating the difference between the measured signal power and the reference signal power (measured with clear sky conditions), similar to the approach utilized by [14]. Moreover, the atmospheric gas absorption is calculated using ITU-R P.676 [16] and is also subtracted from the difference. Since the link is to a GEO satellite, the EPL due to atmospheric absorption is relatively stable over time. Accordingly, the recorded data in each site uses the EPL time vector which corresponds to purely the rain attenuation effect.

To compare the EPL against different rain conditions, the corresponding rain rate data was also collected at each of the sites. Hence, the sites are also equipped with rain sensors capable of measuring the rain rate. Note that in order to maintain the accuracy of the model, the rain data needs to be measured in harmony with the power measurements, i.e., the rain sensor is synchronized with the receiver. Thus, the measurement data-sets include both time vectors of the EPL and rain rate measurements sampled with the same sampling intervals.

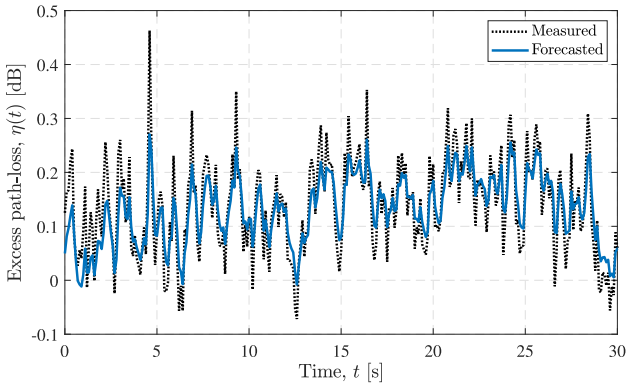

FIGURE 9. Comparison between the measured and the forecasted time-series EPL. The forecasted EPL is obtained using the model-based LSTM with a prediction window of 100ms.

TABLE 2. AlphaSat site measurement information.

Site	Cilbolton	Vigo	Budapest
Country	UK	Spain	Hungary
Latitude [°]	51.15	42.17	47.48
Longitude [°]	-1.43	-8.69	19.06
h_r [km]	2.75	5.23	3.01
h_s [km]	0.10	0.45	0.31
θ [°]	26.40	30.60	35.00
f_c [GHz]	39.04	39.04	39.04
T_s [s]	0.10	0.08	0.10

B. REAL-TIME PREDICTION PERFORMANCE RESULTS

We follow the methodology detailed in Sec. III-B to train the real-time prediction network using the data obtained from the measurements of the three different sites. After the network is trained, the testing data is then injected to the neural network

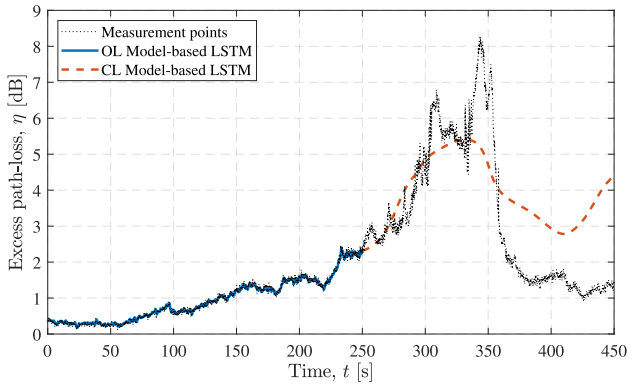

FIGURE 10. Comparison between the measured and forecasted time-series EPL using both the open-loop (0-300s) and closed-loop (300-600s) prediction. The forecasted EPL is obtained using the model-based LSTM.

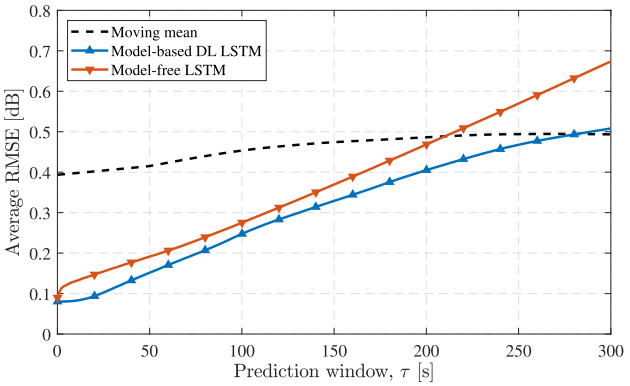

FIGURE 11. Comparison of the RMSE with respect to the real measurements obtained from the different models for a variable prediction window. The proposed model-based DL LSTM demonstrates better prediction accuracy than the conventional model-free LSTM and moving mean as the prediction time window increases.

to verify its performance. Fig. 9 illustrates the prediction accuracy of the model-based deep learning method (black) compared to the measured values (blue). The prediction window is 100 ms (equal to the sampling time) or one sample, where the network is constantly being updated with the measured value in its next prediction iteration, i.e., open-loop prediction.

Moreover, we assess the accuracy of the proposed method for higher prediction windows to examine the model performance as it transitions from short- to medium-term prediction. This is achieved through closed-loop prediction, where the network is not updated with any real measurements to adjust until the prediction window elapses. Fig. 10 illustrates an example for both the open- and closed-loop predictions using the model-based LSTM model using Q/V-band measurements collected at Chilbolton. The accuracy of the real-time prediction model is assessed by examining the error function, i.e. the difference between the predicted and the measured rain fading EPL. A good tool that measures the prediction accuracy is the Root Square Mean Error (RMSE) obtained for a prescribed prediction window τ as follows

$$\mathrm{RMSE}(\tau) = \sqrt{\frac{1}{W}\sum_{n=1}^{W} |\hat{\eta}_n - \tilde{\eta}_n|^2}, \tag{19}$$

where W is the total number of samples in a prediction window of τ seconds. The RMSE changes with the forecasting window and deteriorates as the window size increases. To obtain a more statistically indicative measure, we average the RMSE obtained over different measurements for the same prediction window. The average RMSE as a function of the window duration is illustrated in Fig. 11 for (i) the proposed deep learning model-based LSTM, (ii) one layer LSTM proposed in the literature [31], and the (iii) moving average which relies on regression models [26]. The proposed model-based deep learning LSTM method demonstrates enhanced prediction accuracy of 0.025 dB even with larger prediction windows in comparison to traditional LSTM networks.

C. STATISTICAL CHANNEL MODEL RESULTS

To assess the validity of the time-series generated from the statistical channel simulator, we utilize the GEO measurements and infer them on a simulated LEO satellite pass. First, to obtain the correlation time curve, the measured EPL is divided into smaller segments (e.g., 1 hour intervals) with equal sample size and the autocorrelation for each segment is calculated as follows

$$\hat{r}_k = \frac{\sum_{i=1}^{T-k}(s_i - \bar{s})(s_{i+k} - \bar{s})}{\sum_{i=1}^{T}(s_i - \bar{s})^2}, \tag{20}$$

where $s = \{\tilde{\eta}_1, \tilde{\eta}_2, \ldots, \tilde{\eta}_T\}$ represents a segment of measurements, T is the total number of samples in a measurement segment, $\bar{s}$ is the EPL mean per segment, and k is the lag number. The obtained autocorrelation is exponential in nature and can be fitted using the model in (16) to obtain each segment's corresponding correlation time.

The correlation time vector obtained is then binned into different categories depending on its associated segment average rain rate. The correlation times per bin are then averaged to obtain the correlation time as function of the rain rate. For our measurements, we found that the relationship between the rain rate and the correlation time can be represented by a linear fit function as follows

$$\tau_{\mathrm{cor}}(t) = c_4 R(t) + c_5, \tag{21}$$

where c_4 and c_5 represent the fitting constants of the relationship as a function of r, since the rain rate is time-varying, then the corresponding channel correlation time is also time-variant. The correlation time curve provides the filter with the required correlation time as a function of the LEO satellite pass. Note that all the fitting constants in this paper for the three different sites are listed in Appendix C.

In parallel, the uncorrelated EPL random process is generated based on the LEO elevation angle and measured rain rate. Then, the uncorrelated random process is time-correlated using the correlation filter to obtain the projected GEO measurements on a LEO satellite pass. Fig. 12 illustrates an

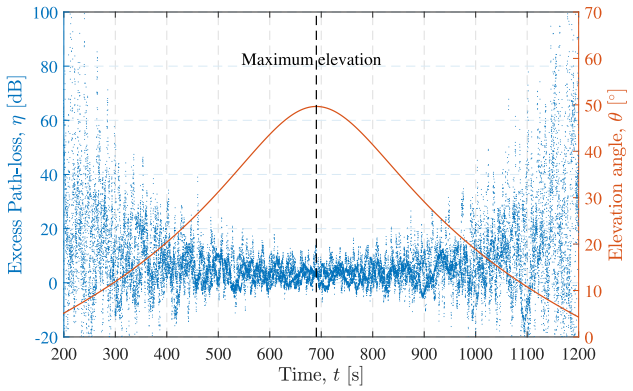

FIGURE 12. An example channel prediction using the channel statistical simulator for one LEO satellite pass with a maximum elevation angle of 50° and altitude of 1,200 km. The predicted EPL is plotted in blue whereas the elevation angle is plotted in red.

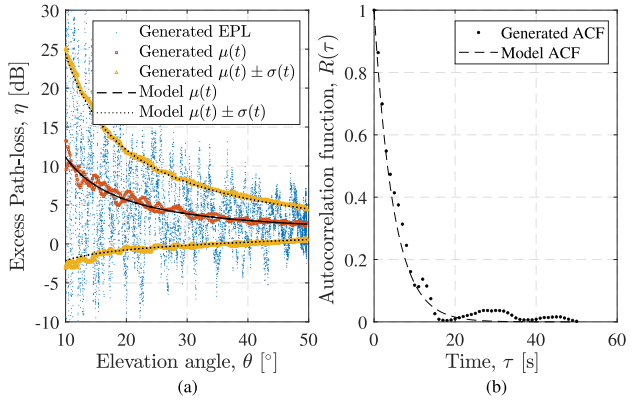

FIGURE 13. Validation of the generated EPL from the channel generator, parameters of which are in Fig. 12, showcasing the close fit of the (a) time-varying statistics and (b) correlation of the generated and model.

example of the time-series generated using the statistical channel simulator for a simulated LEO satellite pass with a maximum elevation angle of 50° and an altitude of 1,200 km. Note that the resulting path loss increases in variability as the elevation angle decreases. The resulting time-series preserves the statistics while maintaining the induced time-correlation as validated in Fig. 13.

VI. CONCLUSION

With the current accelerating rate of satellite network deployments, radio spectrum is becoming more congested with different communication services. New spectral regions in the Q/V-bands are expected to offer superior bandwidth for next generation satellite networks. Despite the availability of this band, both the magnitude and the variability of the channel losses are increased in high frequency bands. In this work, we provided two approaches to capture the effect of weather fading in the Q/V-band for LEO satellite links. The first approach is a forecasting method using model-based deep learning, intended for real-time operation of satellite terminals providing an enhancement of 50% in comparison to traditional deep learning prediction methods. The second approach relies on a statistical channel simulator that generates the path loss as a time-series random process, intended for system design and research. We validated both approaches by capitalizing on real satellite measurements that are obtained from AlphaSat's Q/V-band transmitter at different geographic latitudes. Furthermore, we advocate for a public Q/V-band LEO satellite platform to be developed in the near future to provide measurements at wider elevation angles.

APPENDIX A
PROOF OF (3)

The distance is typically expressed as a function of the global zenith angle by using the cosine rule as follows

$$d(\varphi) = \sqrt{R_{\oplus}^2 + a^2 - 2R_{\oplus} a \cos\varphi}, \tag{22}$$

where φ is the global zenith angle. Using both the sine rule and the total sum of a triangle's angles, we can equate the global zenith angle to the elevation angle with the following relationship [8]

$$\varphi = \frac{\pi}{2} - \theta - \text{asin}\left(\frac{R_{\oplus}}{a}\cos\theta\right). \tag{23}$$

By invoking the trigonometric relationship of the shifted cosine function, we obtain the simplified version present in (3).

APPENDIX B
PROOF OF (6) AND (7)

The mean rain fading is modeled as follows

$$\mu(\theta) = \gamma_{\mu} L_{\text{s}}(\theta), \tag{24}$$

where $\gamma_{\mu} = akr^{\alpha}$ is the attenuation rate in dB/km [32] and L_{s} is measured in km. Using the geometric relationship, the slant distance that is submerged in rain is obtained as follows

$$L_{\text{s}}(\theta) = \frac{h_{\text{r}} - h_{\text{s}}}{\sin\theta}. \tag{25}$$

By substituting L_{s}, we obtain the simplified relationship presented in (6). On the other hand, the fading standard deviation is modeled as follows

$$\sigma(\theta) = \gamma_{\sigma} L_{\text{G}}(\theta), \tag{26}$$

where $\gamma_{\sigma} = br^{c}$ is the attenuation rate in dB/km and L_{G} is measured in km. Using the geometric relationship between the slant distance and the elevation angle, the horizontal distance is calculated

$$L_G = L_{\text{s}} \cos\theta. \tag{27}$$

By substituting L_{s} and L_{G}, we obtain the simplified relationship presented in (7).

APPENDIX C
EMPIRICAL MODEL PARAMETERS

Here, we list the values of the empirical model parameters used for the three different sites.

TABLE 3. Empirical model parameters.

Site	Cilbolton	Vigo	Budapest
c_1	0.44	0.21	0.75
c_2	0.30	0.29	1.37
c_3	0.67	0.34	0.05
c_4	-0.12	-0.42	-0.07
c_5	5.38	10.62	2.55

REFERENCES

[1] B. Al Homssi et al., "Next generation mega satellite networks for access equality: Opportunities, challenges, and performance," *IEEE Commun. Mag.*, vol. 60, no. 4, pp. 18–24, Apr. 2022.

[2] *A Communications Alliance Satellite Services Working Group Paper*, Satell. Ind. Spectr. Strategy, Commun. Alliance Ltd, North Sydney, NSW, Australia, 2022.

[3] A. Gharanjik, B. Shankar M. R., P. Arapoglou, and B. Ottersten, "Multiple gateway transmit diversity in Q/V band feeder links," *IEEE Trans. Commun.*, vol. 63, no. 3, pp. 916–926, Mar. 2015.

[4] B. Xue, N. Tong, X. Xu, and X. He, "Dynamical short-term prediction of rain attenuation in W band: A time-series model with simpler structure and higher accuracy," *IEEE Antennas Propag. Mag.*, vol. 61, no. 1, pp. 77–86, Feb. 2019.

[5] A. D. Panagopoulos, P.-D.-M. Arapoglou, and P. G. Cottis, "Satellite communications at KU, KA, and V bands: Propagation impairments and mitigation techniques," *IEEE Commun. Surveys Tuts.*, vol. 6, no. 3, pp. 2–14, 3rd Quart., 2004.

[6] E. Cianca, T. Rossi, A. Yahalom, Y. Pinhasi, J. Farserotu, and C. Sacchi, "EHF for satellite communications: The new broadband frontier," *Proc. IEEE*, vol. 99, no. 11, pp. 1858–1881, Nov. 2011.

[7] B. A. Homssi et al., "Artificial intelligence techniques for next-generation mega satellite networks," 2022, *arXiv:2207.00414*.

[8] B. Al Homssi and A. Al-Hourani, "Optimal beamwidth and altitude for maximal uplink coverage in satellite networks," *IEEE Wireless Commun. Lett.*, vol. 11, no. 4, pp. 771–775, Apr. 2022.

[9] D. Roddy, *Satellite Communications*. New York, NY, USA: McGraw-Hill Education, 2006.

[10] H. Xu, T. S. Rappaport, R. J. Boyle, and J. H. Schaffner, "Measurements and models for 38-GHz point-to-multipoint radiowave propagation," *IEEE J. Sel. Areas Commun.*, vol. 18, no. 3, pp. 310–321, Mar. 2000.

[11] M. Zemba, J. Nessel, L. Luini, and C. Riva, "Three years of atmospheric characterization at Ka/Q-band with the NASA/POLIMI alphasat receiver in Milan, Italy," in *Proc. 12th Eur. Conf. Antennas Propag. (EuCAP)*, Apr. 2018, pp. 1–5.

[12] S. Ventouras, S. A. Callaghan, and C. L. Wrench, "Long-term statistics of tropospheric attenuation from the Ka/U band ITALSAT satellite experiment in the United Kingdom," *Radio Sci.*, vol. 41, no. 2, pp. 1–19, Apr. 2006.

[13] A. Kelmendi, A. Hrovat, A. Švigelj, and M. Mohorcic, "Fade slope analysis of alphasat satellite measurements at Ka and Q bands," in *Proc. 15th Eur. Conf. Antennas Propag. (EuCAP)*, Mar. 2021, pp. 1–5.

[14] S. Ventouras et al., "Assessment of spatial and temporal properties of Ka/Q band Earth–space radio channel across Europe using alphasat Aldo Paraboni payload," *Int. J. Satell. Commun. Netw.*, vol. 37, no. 5, pp. 477–501, Sep. 2019.

[15] M. A. Samad, F. D. Diba, and D.-Y. Choi, "A survey of rain fade models for Earth–space telecommunication links—Taxonomy, methods, and comparative study," *Remote Sens.*, vol. 13, no. 10, p. 1965, May 2021.

[16] *Attenuation By Atmospheric Gases P Series Radiowave Propagation*, document ITU-R P.676-11, Recommendation, 2016.

[17] *Propagation Data and Prediction Methods Required for the Design of Earth-Space Telecommunication Systems*, document ITU-R P.618, Recommendation, 2017.

[18] *Attenuation Due to Clouds and Fog*, document ITU-R P.840, Recommendation, 2019.

[19] *Study on New Radio (NR) to Support Non-Terrestrial Networks*, 3GPP, Sophia Antipolis, France, Jul. 2020.

[20] P. M. Kalaivaanan, A. Sali, R. S. A. Raja Abdullah, S. Yaakob, M. Jit Singh, and A. M. Al-Saegh, "Evaluation of Ka-band rain attenuation for satellite communication in tropical regions through a measurement of multiple antenna sizes," *IEEE Access*, vol. 8, pp. 18007–18018, 2020.

[21] C. Lu et al., "A new rain attenuation prediction model for the Earth-space links," *IEEE Trans. Antennas Propag.*, vol. 66, no. 10, pp. 5432–5442, Oct. 2018.

[22] T. Maseng and P. Bakken, "A stochastic dynamic model of rain attenuation," *IEEE Trans. Commun.*, vol. COM-29, no. 5, pp. 660–669, May 1981.

[23] C. Kourogiorgas and A. D. Panagopoulos, "A rain-attenuation stochastic dynamic model for LEO satellite systems above 10 GHz," *IEEE Trans. Veh. Technol.*, vol. 64, no. 2, pp. 829–834, Feb. 2015.

[24] Z. Qu, G. Zhang, H. Cao, and J. Xie, "Stochastic dynamic modeling of rain attenuation: A survey," *China Commun.*, vol. 15, no. 3, pp. 220–235, Mar. 2018.

[25] S. B. Matondo and P. A. Owolawi, "FSO rain attenuation prediction using non-linear least square regression," in *Proc. Int. Multidisciplinary Inf. Technol. Eng. Conf. (IMITEC)*, Nov. 2019, pp. 1–5.

[26] A. Mauludiyanto, G. Hendrantoro, M. H. Purnomo, T. Ramadhany, and A. Matsushima, "ARIMA modeling of tropical rain attenuation on a short 28-GHz terrestrial link," *IEEE Antennas Wireless Propag. Lett.*, vol. 9, pp. 223–227, 2010.

[27] S. N. Livieratos and P. G. Cottis, "Rain attenuation along terrestrial millimeter wave links: A new prediction method based on supervised machine learning," *IEEE Access*, vol. 7, pp. 138745–138756, 2019.

[28] M. N. Ahuna, T. J. Afullo, and A. A. Alonge, "Rain attenuation prediction using artificial neural network for dynamic rain fade mitigation," *SAIEE Afr. Res. J.*, vol. 110, no. 1, pp. 11–18, Mar. 2019.

[29] A. Cornejo, S. Landeros-Ayala, J. M. Matias, F. Ortiz-Gomez, R. Martinez, and M. Salas-Natera, "Method of rain attenuation prediction based on long–short term memory network," *Neural Process. Lett.*, vol. 54, pp. 2959–2995, Feb. 2022.

[30] L. Bai, C. Wang, Q. Xu, S. Ventouras, and G. Goussetis, "Prediction of channel excess attenuation for satellite communication systems at Q-band using artificial neural network," *IEEE Antennas Wireless Propag. Lett.*, vol. 18, no. 11, pp. 2235–2239, Nov. 2019.

[31] L. Bai, Q. Xu, S. Wu, S. Ventouras, and G. Goussetis, "A novel atmosphere-informed data-driven predictive channel modeling for B5G/6G satellite-terrestrial wireless communication systems at Q-band," *IEEE Trans. Veh. Technol.*, vol. 69, no. 12, pp. 14225–14237, Dec. 2020.

[32] *Specific Attenuation Model for Rain for Use in Prediction Methods*, document ITU-R P.838, Recommendation, 2005.

[33] M. Domb and G. Leshem, "Rain attenuation prediction for 2.4–72 GHz using LTSM, an artificial recurrent neural network technology," in *Proc. Int. Conf. Electr., Commun., Comput. Eng. (ICECCE)*, Jun. 2021, pp. 1–6.

[34] D. Jacoby, J. Ostrometzky, and H. Messer, "Short-term prediction of the attenuation in a commercial microwave link using LSTM-based RNN," in *Proc. 28th Eur. Signal Process. Conf. (EUSIPCO)*, Jan. 2021, pp. 1628–1632.

[35] G. Maral, M. Bousquet, and Z. Sun, *Satellite Communications Systems: Systems, Techniques and Technology* (Wiley Series in Communication and Distributed Systems). Hoboken, NJ, USA: Wiley, 2011.

[36] A. Al-Hourani and I. Guvenc, "On modeling satellite-to-ground path-loss in urban environments," *IEEE Commun. Lett.*, vol. 25, no. 3, pp. 696–700, Mar. 2021.

[37] *Reference Standard Atmospheres*, document ITU-R P.835-6, Recommendation, 2017.

[38] S. Hochreiter and J. Schmidhuber, "Long short-term memory," *Neural Comput.*, vol. 9, no. 8, pp. 1735–1780, Nov. 1997.

[39] D. P. Kingma and J. Ba, "Adam: A method for stochastic optimization," 2014, *arXiv:1412.6980*.

[40] MATLAB. *Deep Learning Toolbox*. Accessed: Jan. 10, 2023. [Online]. Available: https://au.mathworks.com/products/deep-learning.html

[41] *Parallel Computing Toolbox*. Accessed: Jan. 10, 2023. [Online]. Available: https://au.mathworks.com/products/parallel-computing.html

[42] *Statistics and Machine Learning Toolbox*. Accessed: Jan. 10, 2023. [Online]. Available: https://au.mathworks.com/products/statistics.html

[43] (2022). *V-band ML Channel Model*. Accessed: Jan. 10, 2023. [Online]. Available: https://github.com/bhomssi/Vband_ML_Channel_Model

[44] M. Matsumoto and T. Nishimura, "Mersenne twister: A 623-dimensionally equidistributed uniform pseudo-random number generator," *ACM Trans. Model. Comput. Simul.*, vol. 8, no. 1, pp. 3–30, Jan. 1998.

[45] *Propagation Data Required for the Design Systems in the Land Mobile-Satellite Service*, ITU-R document P.681-11, Recommendation, 2019.